Critical evaluation of electron microscope evidence for order in glassy polymers

Edwin L. Thomas and Eric J. Roche*

Polymer Science and Engineering Department, University of Massachusetts, Amherst, Massachusetts 01003, USA

(Received 9 February 1979; revised 14 May 1979)

INTRODUCTION

High resolution transmission electron micrscopy (t.e.m.) has been recently applied to the study of order in noncrystalline solids. Since scattering methods yield only statistical data averaged over the entire specimen, structure determination by direct imaging presents the possiblity of the investigation of local regions of order in a disordered matrix and can yield information unobtainable by other means.

In 1967, Yeh and Geil[1] suggested, largely on the basis of dark field electron microscopy observations, that ordered regions (so called 'nodules') existed in glassy poly(ethylene terephthalate). This initial work has been followed by other investigations on atactic and isotactic polystyrene[2], polycarbonate[2-5], polybutadiene[6] and polymethyl methacrylate[2] and all of these nominal 'amorphous' polymers have been found to have similar nodular structures with diameters ranging from 2–20 nm. Parallel to, and quite apart from, this polymer work are the more recent observations of order (so called 'microcrystallites') in amorphous semiconductors and amorphous metals. These observations date from 1971, when Rudee[7] suggested, again on the basis of dark field observations, that 'amorphous' germanium consisted of very small wurtzite crystals. A number of subsequent experimental and theoretical investigations have followed which have resulted in a deeper appreciation of the complex problems of image interpretation of disordered solids[8-10].

The original interpretations[1,7] of local order in noncrystalline materials were based on the observation of bright areas in the dark field image (usually formed with scattered electrons from the first diffuse diffraction halo, see *Figure 1*). These bright areas are interpreted as regions in the specimen which are sufficiently ordered to diffract coherently. The size of the bright region in the dark field image is taken as the size of the ordered region. This approach is based on the well developed theory of dark field image interpretation for large crystals, but as we shall see, the extension of this interpretation to image features less than about 3 nm in diameter is not at all straightforward. In addition to the direct observation of order in amorphous polymers by dark field microscopy, there is also evidence for order in amorphous polymers from radiation damage induced changes in the electron diffraction pattern[11] and from electron diffraction studies of liquid polyethylene films[12]. Bright field micrographs of metal-shadowed polymer samples also exhibit

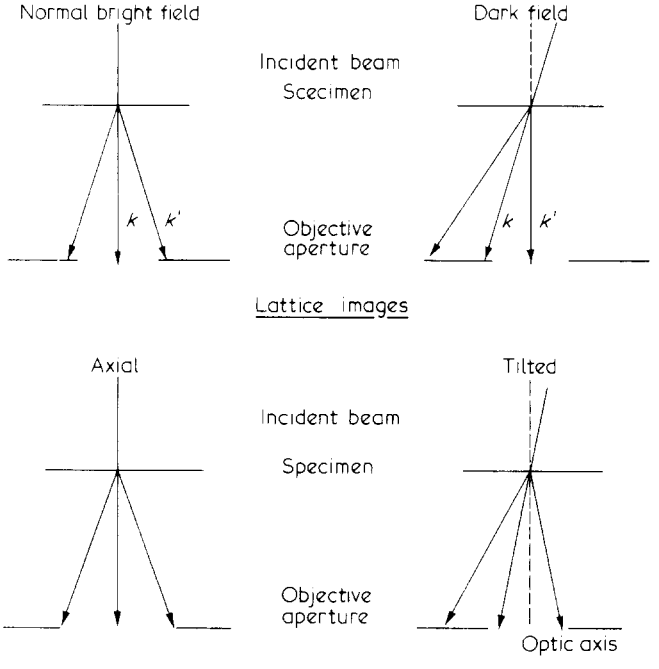

Figure 1 Optical configuration in the electron microscope for different imaging conditions

rough surface structure on the same scale as the domain size but no direct relationship with the bright regions observed *via* dark field has been established.

Both tilted and axial bright field lattice imaging techniques (see *Figure 1*) have been applied to structural studies of amorphous semiconductors and metals, but since the domains in amorphous polymers are not expected to consist of perfectly ordered chains, lattice imaging techniques have not been attempted. Furthermore, the radiation induced defects would make such lattice fringe observations quite difficult, even for sufficiently ordered domains. In his initial dark field work, Rudee suggested 1.4 nm diameter wurtzite microcrystals existed in amorphous Ge. Work with higher resolution instruments has since yielded smaller bright spots in dark field (0.5 nm diameter) which were interpreted again as still smaller microcrystallites[13]. Further support for the microcrystallites in Ge came from bright field lattice imaging, which showed small patches of fringes which were interpreted as the crystallite lattice planes[14]. However, such fringes could also be shown to arise from relatively ordered regions within a continuous random network model[8].

* Permanent address: Centre de Recherches sur les Macromolecules Végétales (CNRS) 53X, 38041 Grenoble Cédex, France

0032–3861/79/111413–10$02.00

Krakow and Ast[15] showed that the inelastically diffracted electrons actually account for the fringes observed in amorphous Ge. For tilted lattice imaging, two sets of fringes due to mutual interference of the elastic direct and scattered beams and the mutual interference of the inelastic direct and scattered beams are always produced In general (continuous distribution of scattered beams, slight objective lens defocus) there will be many sets of fringes and these will be shifted with respect to one another resulting in no overall fringe contrast. For amorphous samples where the scattering distribution is nonsymmetrical and continuous across the objective aperture, two groups of these many sets of fringes, those originating from the interference of scattered electrons on the achromatic circle with the direct beam will be in correct registry and dominate the observed image contrast, leading to artifact crystallite fringes.

Furthermore, the dark field speckle was shown to be possibly only simple statistical peaking in the image of a random solid[8,9]. Theoretical studies have shown that coherently scattering regions are not incompatible with a random network model[8]. Kinematical image calculations using the Polk continuous random network model and a polycrystalline cluster model (1.5 mm diameter microcrystallites) show qualitatively similar speckle patterns in the dark field image[9]. Moreover, only for extremely thin films (ca. 5 nm for Ge films) is the image of a fully diffracting 1.5 nm diameter microcrystallite embedded in either an amorphous matrix or a random oriented array of 1.5 nm diameter microcrystals discernable. For a 10 nm thick film the microcrystallite image would be obscured by the images of experimental images [for which film thickness is considerable (several tens of nonometers)] may "be nothing but random, frequency filtered noise"![10].

Recently, Uhlman and coworkers have repeated the experiments of Yeh on a number of glassy amorphous polymers[16,17]. They arrive at the conclusion that no real ordered structure can be associated with the dark field images of amorphous polymer films. However, though this conclusion is consistent with the evidence to be presented in this paper, no convincing arguments for their assertions are presented and, moreover, their paper presents questions concerning the image formation process in the electron microscope.

It is therefore appropriate to reexamine previous electron microscope investigations of order in amorphous polymers critically in the light of these recent developments.

Transfer theory of image formation

In order for the reader to appreciate the complexities and problems of image interpretation of disordered solids, we present here a brief outline of the transfer theory of imaging (in one dimensional form for simplicity). More extensive treatments of the subject may be found in other texts[18–22].

In the electron microscope, the incident wave (assumed coherent and of amplitude unity) is modulated on passing through the specimen to give the electron wave in the object plane, $F_0(r_0)$.

The image formation can then be expressed as resulting from two successive Fourier transforms First, the object scattering distribution in the back focal plane (b.f.p.) is the Fourier transform of the object function. Second, the image function is given by the Fourier transform of this scattering distribution.

The object scattering function is expressed as:

$$F_0(K) = \int_{-\infty}^{+\infty} F_0(r_0) e^{2\pi i K \cdot r_0} \, dr_0 \tag{1}$$

where $\underset{\sim}{K}$ is the difference scattering vector between the incident wave vector k and the scattered wave vector k', i.e. $|\underset{\sim}{K}| = |\underset{\sim}{k}' - \underset{\sim}{k}| = 2\sin\theta^*/\lambda$. The imperfections of the microscope imaging system can be expressed in terms of a generalized transfer pupil function $P(K)$ so that the effective scattering distribution $F_0'(K)$ in the b.f.p. is:

$$F_0'(K) = P(K) \int_{-\infty}^{+\infty} F_0(r_0) e^{2\pi i K \cdot r_0} dr_0 \tag{2}$$

$P(K)$ can be expressed as

$$P(K) = A(K) e^{i\chi(K)} \tag{3}$$

where $A(K)$ represents the effect of the objective aperture in the b.f.p. of the objective lens and is for a circular aperture centered on the optic axis:

$$A(K) = \begin{cases} 1 \text{ if } |K| < K_{max} \\ 0 \text{ if } |K| \geqslant K_{max} \end{cases} \tag{4}$$

$\chi(K)$ is the phase shift produced by aberrations and defocus in the imaging system. If only spherical aberration and defocus are considered:

$$\chi(K) = \pi\lambda(\Delta Z)K^2 + \frac{\pi}{2} C_s \lambda^3 K^4 \tag{5}$$

where ΔZ is the amount of defocus, C_s is the spherical aberration coefficient of the objective lens, λ is the wavelength of the electrons and K is defined as before†. Then the image function is:

$$F_i(r_i) = \int_{-K_{max}}^{K_{max}} F_0(K) P(K) e^{-2\pi i K \cdot r_i} dK \tag{6}$$‡

For an object composed of N atoms located at object coordinates r_j, $F_0(r_0)$ may be written as

$$F_0(r_0) = \sum_{j=1}^{N} f_j \delta(r_0 - r_j) \tag{7}$$

where f_j is the atomic scattering factor for electrons for the jth atom. $F_0(K)$ then becomes

* θ is half of the scattering angle

† This is true if K is parallel to the optic axis, if not, χ is expressed as a function of α, the angle between the scattered beam and the optic axis and is $\chi(\alpha) = \pi/\lambda(\Delta Z\alpha^2 + C_s\alpha^4/2)$

‡ The position vector r_i in the image plane is related to the object plane coordinates by $-r_i/M = r_0$ where M is the magnification. For convenience we take $M = 1$ and use the inverse Fourier transform notation to take care of the image inversion

$$F_0(K) = \int_{-\infty}^{+\infty} \sum_j f_j \delta(r_0 - r_j) e^{2\pi i K \cdot r_0} dr_0 \quad (8)$$

which gives the familiar result

$$F_0(K) = \sum_j f_j e^{2\pi i K \cdot r_j} \quad (9)$$

The image function is then

$$F_i(r_i) = \int_{-K_{max}}^{K_{max}} \sum_j f_j e^{2\pi i K (r_j - r_i)} e^{i\chi(K)} dK \quad (10)$$

Weak phase object

For light atoms, the atomic scattering factors can be expressed as

$$f_j = 1 + i\rho_j$$

where ρ_j is real and $\ll 1$. For the weak phase object equation (9) becomes:

$$F_0(k) = 1 + i \sum_j \rho_j e^{2\pi i K r_j} \quad (11)$$

whereby the image amplitude is then:

$$F_i(r_i) = 1 + i \int_{-K_{max}}^{+K_{max}} \sum_j \rho_j e^{2\pi i K (r_j - r_i)} e^{i\chi(K)} dK \quad (12)$$

which can be written as

$$F_i(r_i) = 1 + \psi_S \quad (13)$$

where 1 is the transmitted amplitude function (equal to the incident function) and ψ_S is the scattered amplitude function. The image intensity is then

$$I(r_i) = |1 + \psi_S|^2 \quad (14)$$

Bright field image for a weak phase object

Since the scattered intensity is very weak with respect to the transmitted intensity,

$$I_{BF} \simeq 1 + \psi_S + \psi_S^* \quad (15)$$

where ψ_S^* is the complex conjugate of ψ_S

or

$$I_{BF}(r_i) \simeq 1 - i \int_{K_{max}}^{+K_{max}} \sum_1 \rho_1^* e^{-2i\pi K \cdot (r_1 - r_i)} e^{-i\chi} dK + i \int_{-K_{max}}^{+K_{max}} \sum_j \rho_j e^{2i\pi K (r_j - r_i)} e^{i\chi} dK \quad (16)$$

Assuming for simplicity only one type of atom,

$$I_{BF} = 1 + N_\rho \int_{-K_{max}}^{+K_{max}} \sum_m \frac{1}{i} (e^{-[2i\pi K (r_m - r_i) + i\chi]} - e^{[2i\pi K (r_m - r_i) + i\chi]}) dK \quad (17)$$

or

$$I_{BF} = 1 - 2N_\rho \int_{-K_{max}}^{+K_{max}} \sum_m \sin[2\pi K (r_m - r_i) + \chi] dK \quad (18)$$

which finally yields the bright field image intensity for a weak phase object:

$$I_{BF} = 1 - 2N_\rho \int_{-K_{max}}^{+K_{max}} \sum_m \cos 2\pi K (r_m - r_i) \sin\chi(K) dK \quad (19)$$

Treatment in two dimensions leads to the same expression (19) where $\underset{\sim}{K}$, $\underset{\sim}{r}_m$ and $\underset{\sim}{r}_i$ are now vectors.

For the axial bright field image of a weak phase object, effects of aberration and defocus appear simply as sin χ, the so-called microscope 'transfer function' which modulates the Fourier components contributing to the bright field image. Image contrast in this case arises from the *linear* superposition of the modulated Fourier components.

Sin χ is a sensitive function of the objective lens defocus and will cause contrast reversal and alternatively highlight or suppress particular object frequencies in the image (see *Figure 2*). The above treatment has assumed coherent illumination. The effect of beam divergence as well as voltage and current fluctuations has been shown essentially to decrease the maxima of the transfer function, especially at high resolution[20]. The transfer function has been shown to account for the observed 'salt and pepper' structures of thin amorphous carbon films[23,24]. The scale of the phase contrast structures observed and their contrast was shown to depend on the defocus of the objective lens and the high frequency cut off of the objective aperture (K_{max}). Calculated bright field images of pure noise objects (e.g. objects with a continuous spatial frequency spectrum) are qualitatively indistinguishable from experimental images obtained from evaporated carbon films under the same transfer function conditions[23]. A number of published bright field micrographs of amorphous polymer samples appear qualitatively similar to these salt and pepper images. The origin of the observed contrast in the range 2 to 4 nm has been previously (erroneously) suggested to be due to diffraction contrast from ordered regions[25] or to the high frequency cut off of the objective aperture[16,17]. The objective aperture serves to limit the range of the spatial frequencies present in the image but does not influence their contrast. The contrast of a particular object frequency depends only on the value of sin χ for that frequency.

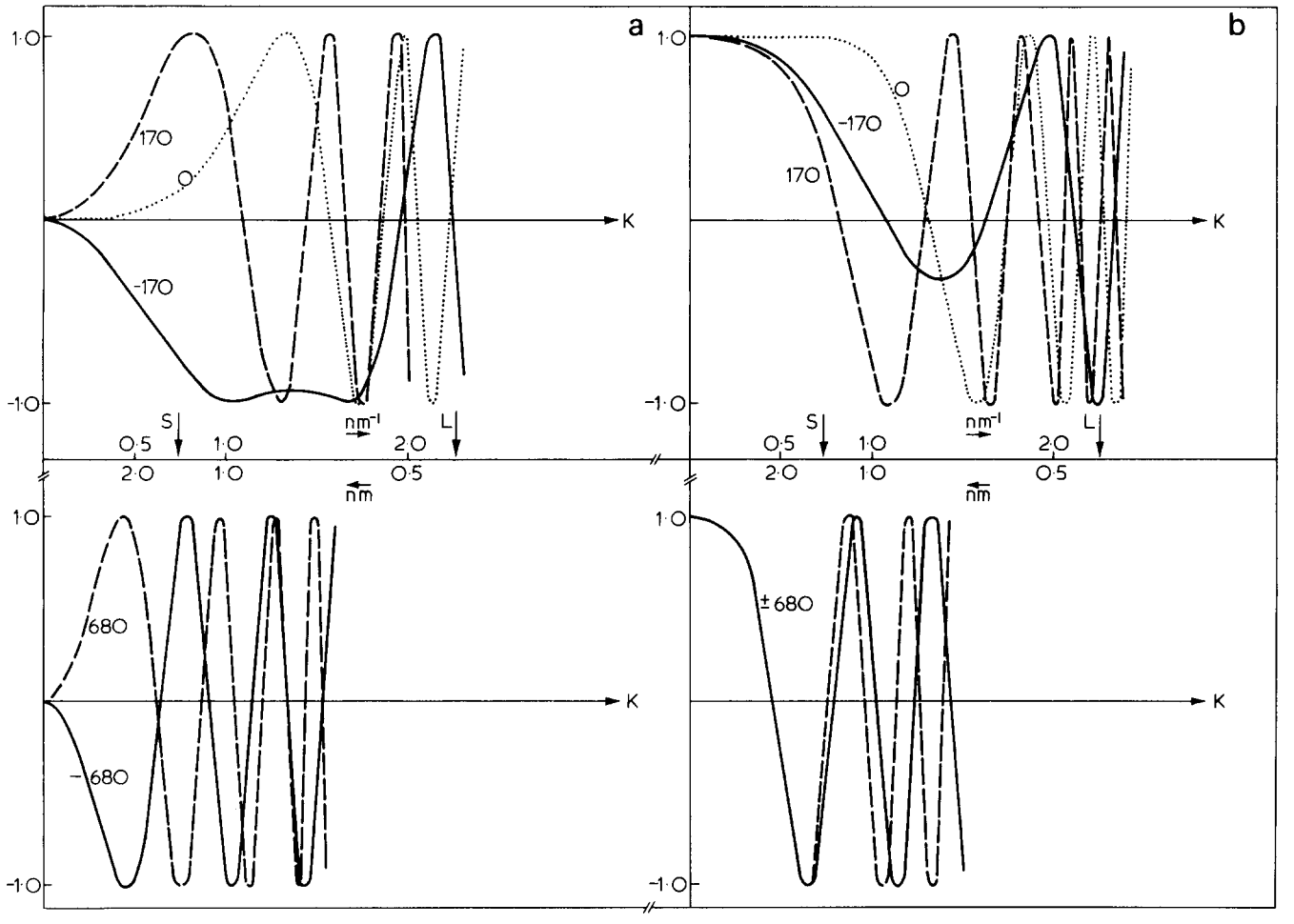

Figure 2 Variation of the sin χ and cos χ functions with defocus (values indicated on the curves in nm); C_s = 6.5 mm. Arrows indicate the smallest K values selected by the large (L) and small (S) apertures

Figure 3 shows a three step through-focus series of a thin atactic polystyrene film. A close inspection of *Figures 3a* and *3c* shows that regions (indicated by arrows) which are bright in the overfocused image have become dark in the underfocused image and vice versa (this is because sin χ is an odd function of Δz). The effect of the transfer function on the image contrast is quite marked for $\Delta z \simeq 0$, since now sin χ is very small for the low frequencies and oscillates strongly at high object frequencies so that the strong transfer intervals become very narrow and the visible image structure is very fine scale. Light optical Fraunhofer diffraction patterns of bright field electron micrographs show the power spectrum of image intensity as affected by the microscope transfer function as a function of the objective lens defocus. The optical diffractogram intensity distribution $I(\underset{\sim}{h})$ is the square of the Fourier transform of the electron micrograph image intensity distribution,

$$I(\underset{\sim}{h}) = |\int I_{BF}(\underset{\sim}{r}_i) e^{2\pi i \underset{\sim}{h}\underset{\sim}{r}_i} \, d\underset{\sim}{r}_i \, |^2 \qquad (20)$$

For an object with a uniform spatial frequency spectrum any anisotropy in $I(\underset{\sim}{h})$ is due to astigatism, drift, aperture misalignment, etc. and the zeros (spatial frequency gaps) of $I(h)$ are determined by the zeros of $\sin^2\chi$. The optical diffractogram in *Figure 4* indicates a high quality image and shows the variation of $\sin^2\chi$ with objective lens defocus (Δz = 680 nm here). Good correspondence is found between the calculated and observed transfer function. Only slight anisotropy is present and up to 5 maxima are observed with decreasing intensity due to the effect of beam divergence on the transfer function. The behaviour and appearance of the axial bright field micrographs of thin atactic polystyrene films are therefore entirely consistent with microscope transfer function modulated images of an amorphous sample acting as a weak phase object.

Dark field image

For the tilted incident beam dark field image the situation is more complicated (see *Figure 5*). The incident beam $\underset{\sim}{k}$ now makes an angle β with the optic axis which is denoted by the vector $\bar{k}$. The difference scattering vector $\underset{\sim}{K}$ is still $\underset{\sim}{k}' - \underset{\sim}{k}$, but now the microscope phase shift χ depends no more on $\underset{\sim}{K}$ but on $k' - \bar{k}$. The dark field image intensity is then given by $\psi_s \psi_s^*$:

$$I_{DF}(\underset{\sim}{r}_i) = \rho^2 \int_{\underset{\sim}{K}} \int_{\underset{\sim}{K}} \sum_j \sum_l e^{2\pi i[\underset{\sim}{K}\cdot(\underset{\sim}{r}_j - \underset{\sim}{r}_i) - \underset{\sim}{K}'\cdot(\underset{\sim}{r}_l - \underset{\sim}{r}_i)]} e^{i[\chi(\underset{\sim}{K}+\underset{\sim}{K}_0) - \chi(\underset{\sim}{K}'+\underset{\sim}{K}_0)]} \, d\underset{\sim}{K} d\underset{\sim}{K}' \qquad (21)$$

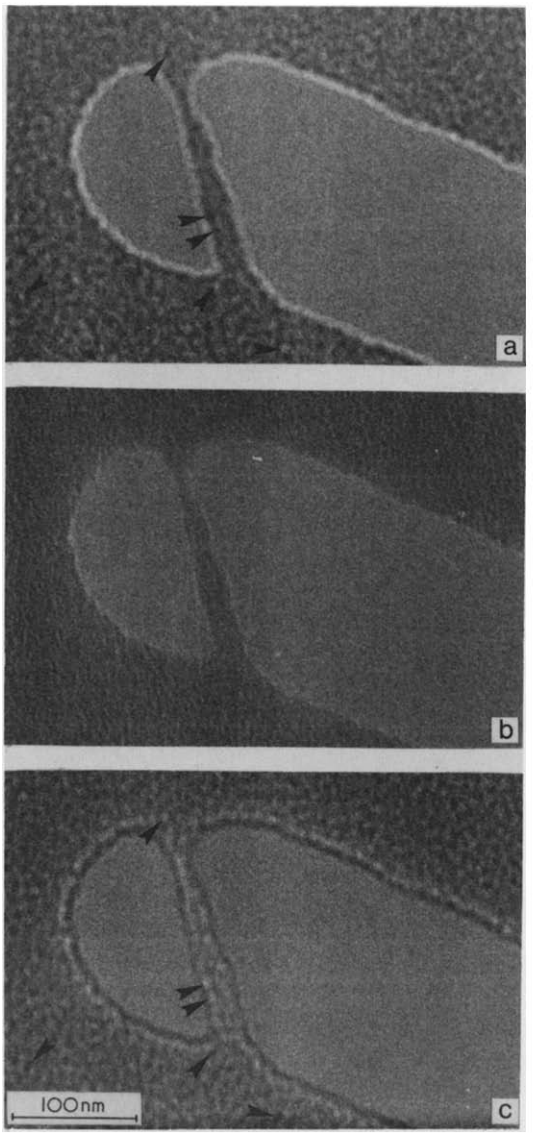

Figure 3 Bright field through focus series images of a thin a-PS film. Defocus is ±680 nm

where $\underset{\sim}{K}_0 = \underset{\sim}{k} - \underset{\sim}{\bar{k}}$. While the image transfer for axial bright field imaging outlined above is linear because only the interferences of the relatively weak scattered beams with the strong unscattered beam are taken into account, the dark field image transfer is nonlinear since now just those contributions from the mutual interferences of all the scattered waves contribute to the image.

The dark field image intensity is therefore the superposition of the scattered components which fall into the objective aperture modulated by the microscope phase shift. Intensity peaks occur due to in-phase combinations at particular r_i in the image plane. These peaks can in general result from:

(1) Ordered regions (domains or microcrystallites – 'real image')

(2) Fortuitous superposition (statistical peaking – 'statistical image')

Howie and Krivanek[9] have calculated dark field images for the two types of models. An 'ideal amorphous' (statistical) sample dark field image was calculated from a 519 Si atom random network developed by Polk[2] and the microcrystallite sample images were calculated using computer generated wurtzite structure polycrystalline aggregates of about 1120 Si atoms in 15 strain-free wurtzite crystals. The crystals are arranged at random, but fit together so that no two atoms are closer than a nearest neighbour distance and so that there are no vacant places large enough to accommodate an extra bonded atom. For the microcrystalline model, one 1.4 nm diameter crystal in the center of the film at the exact Bragg angle. The dark field images were then calculated by computer using essentially equation[21] with the objective aperture centred on the first diffraction halo with the integral over $\underset{\sim}{K}$ now defined by the position of the aperture in the diffraction pattern. The calculated images for both models show qualitatively similar speckle patterns for films > 3 nm thick. The speckle size is in the order of 0.3-0.5 nm which corresponds to the diameter of the Airy disc (determined by the size of the objective aperture employed). At a specimen thickness of about 3 nm both types of model images are dominated by superpositions of atomic images between atoms which are uncorrelated (e.g. further apart than the domain size). Hence it seems unlikely that dark field imaging will distinguish the two types of model when the object thickness is large compared to the domain size. Thus, only if the speckle size observed in the dark field image of a suitably thin film is much larger than the Airy disc size, are the bright spots indicative of significant local ordering in the specimen. [For example, 5 nm speckles observed in a 10 nm thick film would inidcate that real coherent scattering domains are present.] This has not been appreciated in previous dark field studies of polymers.

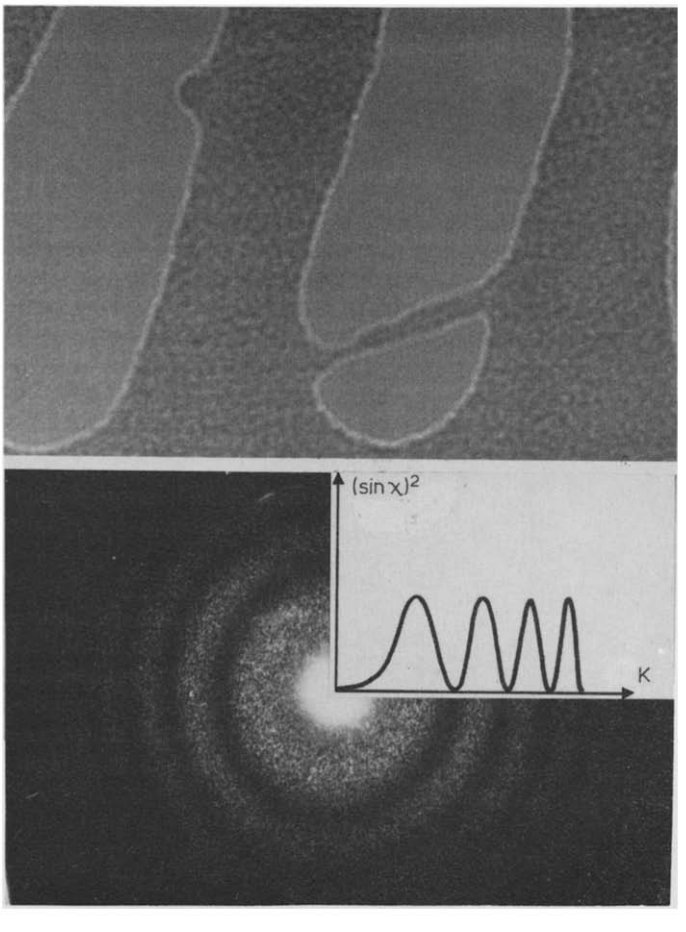

Figure 4 Optical diffractogram and corresponding micrograph ($\Delta Z = -680$ nm). The plot shows the variation of $\sin^2\chi$ with scattering angle

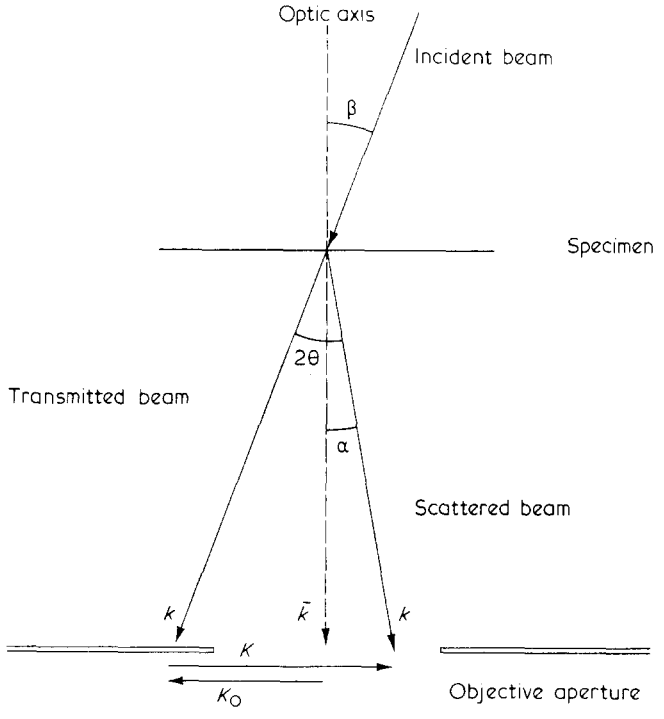

Figure 5 Schematic of the tilted beam dark field imaging technique

Howie and Krivanek have also investigated defocus and sample tilt as possible ways to distinguish the random network from the microstallite model. From equation 21 the effect of defocus is seen just to alter the phases of the scattered components. If the image is due to statistical peaking, a change in focus will just cause new fortuitous combinations to give rise to intensity peaks and hence the bright spots will decrease in intensity, disappear and new spots appear but there will be no change in the average spot size and no single best image focus setting. For images resulting from the presence of real object order, defocusing will just cause the spots to blur if the defocus is larger than the depth of field (about 100 nm for an objective aperture of 10^{-3} radians) but the spots will remain fixed and of constant intensity. The suggestion[17] that the dark field speckle arises from the same mechanism as does the bright field 'salt and pepper' structure, with the implication that this speckle would disappear at exact focus in dark field, is completely wrong.

Recent work by Gibson, Howie and Stobbs[27] has shown that if the dark field image is only partially coherent (corresponding to a range of incident $\underline{k}$) the contributions from larger $\underline{r}_{jl}$ separations are suppressed and speckle from statistical effects is reduced With partially coherent illumination, the speckle also shows an optimal focus because of the dependence of χ on $\underline{k}$ as well as Δz.

Since the incident and scattered wave vectors $\underline{k}$ and $\underline{k}'$ are both very nearly parallel to the optic axis, $K_z \approx 0$ so that the image is rather insensitive to the z_j coordinates of the atoms in the specimen – that is, the image is essentially a reconstruction of a two dimensional projection of the object.

Tilting of the sample can help to sort out the image resulting from overlap of atomic images from that of a diffracting microcrystallite since a given tilt will effect the larger $\underline{r}_{jl}$ correlations more strongly. Controlled tilting experiments are, however, experimentally quite difficult at this resolution and since Δz unavoidably changes with tilt, a through focus series would be needed at each tilt[9].

In summary, dark field image interpretation from disordered samples is quite complicated but in principle with careful control of beam coherence, aperture size, defocus of objective lens and specimen tilt, distinction between real and statistical images is possible for suitably thin specimens.

Previous results on glassy atactic polystyrene

Of the polymers thus far investigated, atactic polystyrene is the most suitable material, because it is noncrystallizable and rather radiation resistant. The original work on atactic polystyrene employed 50 nm thick films cast from a 0.5% benzene solution[2]. The diffraction pattern consisted of 4 diffuse rings ($|\underline{K}| = 1.1, 2.1, 4.5$ and 8.2 nm^{-1}). The 2.1 nm^{-1} ring was reported to broaden irreversibly and shift to 1.6 nm^{-1} at high electron dose. The 2.1 nm^{-1} scattering peak was used exclusively for the published dark field images with a 50 μm aperture. The observed bright speckle varied from 1.5–4.0 nm with an average speckle (domain) size of 2.7 nm. No variation of the size of the spots was observed with increasing irradiation. The 1.1 nm^{-1} peak is thought to be intermolecular and the 2.1 nm^{-1} peak approximately half inter and half intra molecular in origin with the 4.5 and 8.2 nm^{-1} peaks as intramolecular in origin[28]. The recent work[16,17] on atactic polystyrene employed films about 60 nm thick cast from 3.5% methylethyl ketone solution. The sample was also coated with a thin (unspecified thickness) layer of carbon. Dark field images were obtained with a 25 μm aperture centered on the second diffuse halo (the same as used by Yeh). The speckle size observed was about 0.5 nm.

Remarks on high resolution dark field microscopy of polymers

For 'amorphous' polymer specimens which contain molecules randomly arranged in addition to possible (partially) ordered domains, dark field image interpretation becomes an even more intricate problem. That is, the image may contain real features arising from several types of correlated atom separations. Significant intramolecular corrections beyond the first nearest neighbour generally occur in polymer samples (e.g. r_{13} is a constant for carbon-carbon polymer backbone and r_{13}, r_{14} are constants for the phenyl rings, etc.) which will tend to confound the investigation of intermolecular ordering. Moreover, the unavoidable radiation damage due to the large specimen dose necessary for high resolution dark field observations may cause sample mass-loss, loss of order, and general local atomic rearrangements. The total inelastic/elastic scattering cross section ratio is about 2 for carbon[29,30]. so that inelastic contributions are much more important for polymers than for higher atomic number materials where elastic scattering dominates. The inelastic and elastic scattering distributions for amorphous carbon have been calculated by Crick and Misell[30]. For a 5 nm thick* carbon film the inelastic ratio varies from 5/1 to 2.5/1 in the range 1.1 nm$^{-1} \leqslant |K| \leqslant 2.1$ nm^{-1}. These calculations for the elastic scattering distribution do not however include correlations between nearest neighbour atoms (intramolecular order) nor the presence of small ordered regions (intermolecular order) both of which will lead to peaks in the elastic scattering distribution. In order to achieve as high as possible an elastic/inelastic signal the objective aperture should be centred on an elastic scattering peak. Images formed from either intermolecular or intramolecular elastic scattering peaks will contain information about the size and location of the region giving rise to the co-

* The density of amorphous carbon is about 2, hence a 50 nm evaporated carbon film corresponds to approximately a 100 nm polystyrene film.

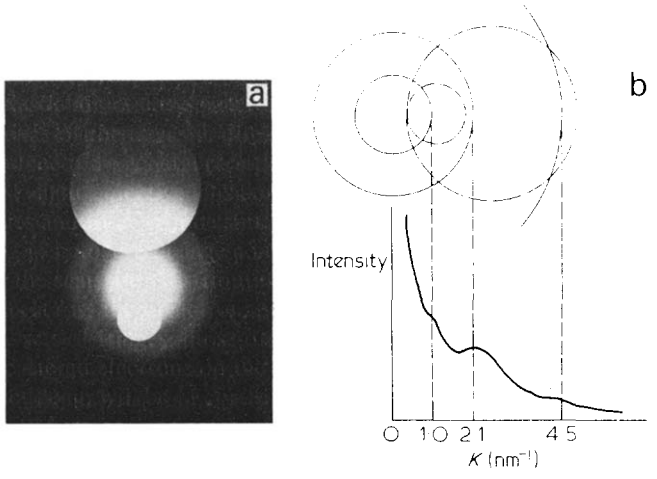

Figure 6 (a) Diffraction pattern showing location of the objective aperture positions; (b) schematic showing range of $\underset{\sim}{K}$ values selected by the two apertures

herent scattering. Dark field micrographs have been obtained for various electron optical conditions in order to critically address the earlier interpretations of local order in this particular polymer glass.

EXPERIMENTAL

The preparation of thin samples suitable for t.e.m. presents problems. As Geil[25] and Uhlmann[16] have pointed out, ion etching (non-uniformity of incident ion flux) of bulk samples suffers from lack of reproducibility and uniformity of film thickness. Ultramicrotomy has not yet been used but the required (<10 nm) thickness for meaningful dark field studies would be extremely difficult to obtain. Solvent casting can produce quite thin films but the conformational restraint at the surfaces (substrate–polymer and polymer–air) may influence the molecular packing. Nevertheless, solvent cast thin film has been used in the majority of the previous dark field studies and presently seems to be the best approach. Thin films of a Pressure Chemical fractionated atactic polystyrene of 670 000 molecular weight with $M_w/M_n < 1.1$ were cast onto clean glass microscope slides from a 0.5 wt% solution of the polymer in toluene. After drying, the films were diced into small pieces and picked up on 300 mesh copper grids for microscopy. The nominal film thickness is estimated to be 20 nm. Micrographs were obtained for regions adjacent to small holes in the film which are extremely thin and provide as well a convenient means to estimate $\Delta z \approx 0$ by the Fresnel Fringe method.

A Jeol 100 CX transmission electron microscope operated at 100 KeV was used in this investigation. Line resolution was tested to be better than 0.34 nm (graphite lattice planes). For the 28 μm and 85 μm diameter objective apertures employed, the Airy disc radius, defined as the distance from the central maximum to the centre of the first zero (e.g. $R_A = 0.61\lambda f/R$) is about 0.9 nm and 0.3 nm respectively. Micrographs were taken with the objective aperture centred on the K = 1.1 and 2.1 nm^{-1} elastic peaks at 50 000 χ using 2–4 sec. exposures. The beam divergence is less than 10^{-3} radians, so that the sample is essentially coherently imaged.

Figure 6a shows the relative position with respect to the transmitted beam of the two apertures used for dark field imaging, as viewed in the back focal plane of the objective lens. For clarity they have been photographed on opposite sides of the main beam. Because of the triple exposure used here the halos appear much more intense inside the apertures than outside so that the 4.5 nm^{-1} halo is almost invisible. In the apertures however, the illumination is well representative of the experimental conditons. *Figure 6b* shows the range of $\underset{\sim}{K}$ selected by these apertures. Typically the 28 μm aperture was approximately centred on the 1.1 nm^{-1} halo but always excluded the 2.1 nm^{-1} halo; the 85 μm aperture selected essentially the 2.1 nm^{-1} halo. In each case the aperture was centred on the optic axis of the microscope by the tilting of the incident beam. We denote these two different aperture conditions as 'S' for the small aperture and 'L' for the large one.

For accurate comparison of successive pictures of the same area under different conditions, a transparant sheet was used where dots from one picture were marked. The transparent sheet could then be superposed on the other pictures and in that way correspondence or non-correspondence of about one hundred dots per image was checked. Small holes in the films were used to register correctly the transparent film and the micrographs.

RESULTS AND DISCUSSION

Provided electron beam radiation damage does not cause significant changes in the atomic positions, a feature to be expected from both real and statistical images is reproducibility under identical optical conditions. Dark field images of atactic polystyrene films were found to be reproducible. *Figures 7a, b* show micrographs of the same area recorded using 'S' aperture conditions with the focus setting corresponding to an approximate in focus bright field image. *Figures 7a* and *7b* were taken under identical conditions with a one minute time interval between exposures during which other images were recorded at different defocus values. *Figure 7b* has somewhat better contrast – this improvement of the dark field image with exposure time was generally observed at the very beginning of the irradiation of the film. It may be related to initial sample mass loss and to the stabilization of the sample mass and diffraction pattern already mentioned

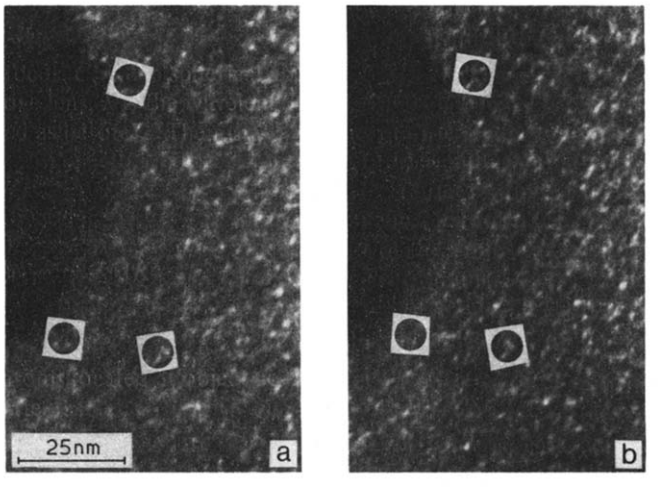

Figure 7 Successive dark field images of atactic polystyrene film recorded under identical conditons attesting good reproducibility. Corresponding typical dot groups are circled

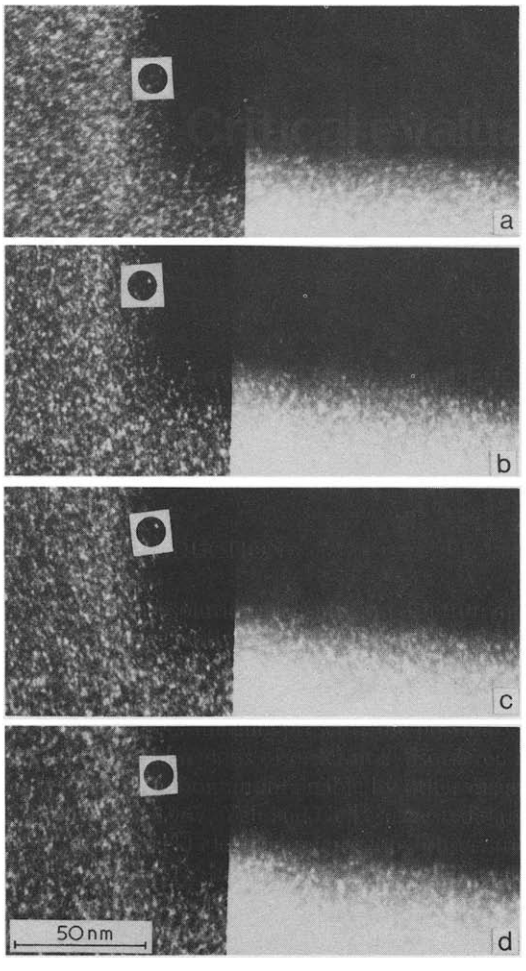

Figure 8 Effect of defocus change on the dark field image of an atactic polystyrene film. (a) $\Delta Z = 0$; (b) $\Delta Z = -170$ nm; (c) $\Delta Z = -340$ nm; (d) ΔZ varied from -510 nm to $+510$ nm; 'S' aperture conditions. The less exposed region is a very thin film area

in the literature[31,32] †. Typical dot groups have been circled to help visual comparison. Using the transparent technique, 80% of the dots in *Figure 7b* are also found in *Figure 7a* with even a better correlation from *7a* to *7b*. This attests to good reproducibility and permits one to study the effect of the microscope parameters on a series of images of the same area.

Another interesting feature of the dark field images of atactic polystyrene films observable in *Figure 7* is the distribution of the number density of the dots as a function of their intensity. In a given area, the number of dots of comparable intensity (visually estimated) increases sharply as their intensity decreases. This agrees well with the theoretical predictions of Krivanek for statistical images[33]. For statistical images, the distribution follows that for a most probable distribution:

$$N(I) = \frac{1}{\bar{I}} e^{-I/\bar{I}} \qquad (22)$$

where $N(I)$ is the number density of dots of intensity I and $\bar{I}$ is the average dot intensity. A Gaussian distribution would be expected for real ordered-domain images.

† It should be noted that the electron dose necessarily employed for high resolution dark field imaging far exceeds the end point dose for sample mass loss and scattering pattern changes.

Figure 8 illustrates the effect of specimen thickness on the dark field image. These images are from extremely thin (circa 5 nm) regions and the micrograph prints have been photographically dodged to show these regions clearly. As film thickness increases away from these regions, the image becomes progressively filled with dots whose apparent size and brightness increase due to superposition effects. The 2.7 nm average domain size observed by Yeh with values up to 4 nm is most probably due to the considerable image superposition in his 50 nm thick films. Measurements in the thinnest regions of our films indicate a dot size in the range 0.7 to 1 nm for 'S' aperture conditions.

Figure 8 also illustrates the effect of variations of the objective lens defocus on the dark field image. The first three micrographs of the series correspond to successive increases of underfocussing by increments of 170 nm from the initial optimal bright field setting. *Figure 8d* was recorded with the focus varied *during* the exposure over a 1020 nm range. As *Figures 8a–8d* show, the size of the dots is not affected by objective lens defocus – behaviour typical of statistical images. The effect of defocus on the intensity and location of the dots is as follows: at relatively small defocus (typically 170 nm) a good correspondence between successive images is found but the intensity of some of the dots is modified. Comparing images with 340 nm change in focus, the proportion of stable dots decreases to about 50% with further changes of the intensity of these stable dots. A few dots appear remarkably stable (circled). A large variation of defocus leads to an almost completely new image in *Figure 8d*. The dots in *Figure 8d* are still sharp even though the focus was varied over 1020 nm. Since the depth of field for these conditions of illumination was only 100 nm, real ordered domain images would have been blurred while the sharpness of a statistical image would be expected to remain unaffected.

Figure 9 shows the effect of aperture size and location on the dark field image. *Figures 9a–9c* are images employing 'L' aperture conditions while *Figure 9d* shows the same area under 'S' aperture conditions. As can be seen in *Figures 9a–9c*, the dark field image is more sensitive to objective lens defocus for a larger objective aperture. There is essentially no correlation between successive 170 nm defocus micrographs in this series. The speckle size is also on the average smaller, slightly less than 0.5 nm and the number of dots per unit area is strongly increased. This unfortunately makes comparison of successive micrographs more difficult, but comparison can be made in the thinnest areas. Arrows point to several large real impurity crystallites which provide a convenient orientation system for the transparency technique and also illustrate perfectly the blurring effect of defocus on real structures. Examination of the small dots indicates again that there is no significant change of their size or sharpness with defocusing.

The bright dot size has been thus found to vary with aperture size (neglecting spurious superposition in thick films). For the apertures employed, the Airy radii 0.3 to 0.9 nm correspond well to the measured spot diameters. The change in spot intensity and location in the image with defocus can be explained from equation (21) by noting that both $\cos\chi$ and $\sin\chi$ (included in the exponential form $e^{i\chi}$) modulate the scattered waves contributing to the image. The behaviour of these functions with defocus has already been described for the axial bright field image case (see *Figure 2*). For tilted beam dark field conditions, the $|\underset{\sim}{K}|$ values of equation (5) must however be shifted by $|\underset{\sim}{K}_0|$. When a new Δz is used

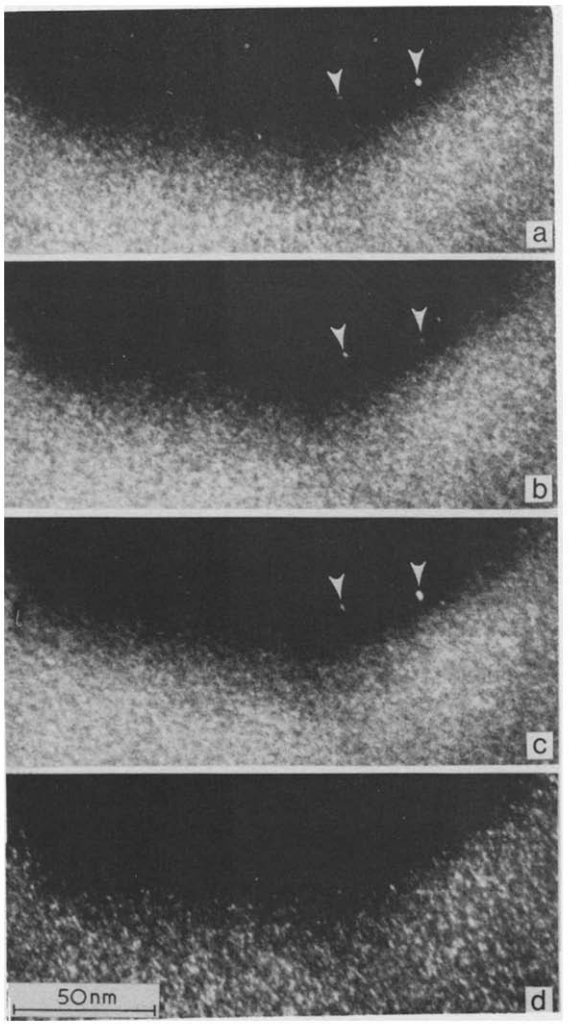

Figure 9 Effect of defocus change on the dark field image with 'L' aperture conditions. (a) $\Delta Z = 0$; (b) $\Delta Z = -170$ nm; (c) $\Delta Z = -340$ nm; (d) same area under 'S' aperture conditions, $\Delta Z = -340$ nm

for the dark field image the $\cos\chi$ and $\sin\chi$ functions modulate the terms in the integral of expression (21) resulting in new in phase combinations leading to a different statistical image. The striking difference between the image response to a given defocus change for 'S' and 'L' apertures may also be understood with reference to equation (21). With the objective aperture centred on the optic axis, the variation of $\cos\chi$ and $\sin\chi$ with defocus is very small for the range of $|\underset{\sim}{K}|$ selected by the small aperture, compared to the dramatic variation of $\cos\chi$ and $\sin\chi$ at higher $|\underset{\sim}{K}|$ for the larger aperture. Thus a smaller defocus value is needed to affect a given change of the image statistics.

The effect of inelastic scattering on dark field image formation is not well understood at present. Most of the inelastic scattering in amorphous carbon is from surface and bulk plasmon losses and therefore this delocalized, incoherent inelastic scattering has been suggested to give rise to a uniform diffuse background intensity which simply superposes with the elastic intensity[34]. Misell and coworkers[35,36] however suggest that for amorphous carbon, and even more so for amorphous insulator polymers like polystyrene, the plasmon losses may be quite localized so that the inelastic component would be imaged at high resolution in a plane separated from the elelastic component by a distance $z_0 = C_c(E_0/E)$ where E_0 is the mean energy loss in the material, E is the incident beam energy and C_c is the chromatic aberration coefficient of the objective lens. Our results for 'S' aperture conditions for which there is a dominant contribution of inelastic scattering to the image tend to support Misell's suggestion since there is no significant increase of the background compared to 'L' aperture conditions.

CONCLUSIONS

We have endeavoured to clarify several misconceptions of both bright field and dark field image interpretation of amorphous polymers. The original basis for the suggestion of ordered domains in glassy amorphous polymers was the observation of small bright dots in the dark field image. We have undertaken several systematic dark field electron optical experiments in order to understand the nature of this speckle. The behaviour of the vast majority of the dots with respect to changes of objective lens defocus and objective aperture size and location in the scattering pattern are entirely consistent with a statistical image rather than a real ordered domain image interpretation. The main result of this investigation is to identify clearly the dark field images as essentially statistical images which may be well understood in terms of the transfer theory of image formation. Visualization of the short range, largely intramolecular order that is present in this system was not possible with the resolution presently obtained. Our results for this particular polymer glass strongly indicate that ordered structures on the scale of 1–10 nm or more do not exist in thin atactic polystyrene films, thus reconciling the electron microscopy studies with the many scattering studies which failed to find evidence for such structures (see for example refs 37–39).

ACKNOWLEDGEMENTS

Acknowledgement is made to the donors of the Petroleum Research Fund, administered by the American Chemical Society and to the Materials Research Laboratory of the University of Massachusetts for partial support of this work. One of us (E.J.R.) thanks the CNRS for the opportunity to work in Amherst.

REFERENCES

1 Yeh, G. S. Y. and Geil, P. H. *J. Macro. Sci. (B)* 1967, **1**, 235
2 Klement, J. J. and Geil, P. H. *J. Macro. Sci. (Phys.) (B)* 1972, **6**, 31
3 Carr, S. H., Geil, P. H. and Baer, E. *J. Macro. Sci. (B)* 1968, **2**, 13
4 Frank, W., Goddar, H. and Stuart, H. A. *J. Polym. Sci. (C)* 1967, **5**, 711
5 Siegmann, A. and Geil, P. H. *J. Macro. Sci. (B)* 1970, **4**, 239
6 Luch, D. and Yeh, G. S. Y. *J. Appl. Phys.* 1972, **43**, 4326
7 Rudee, M. L. *Phys. Stat. Solidi (B)* 1971, **46**, 1
8 Chaudhari, P., Graczyk, J. F. and Charbnau, H. P. *Phys. Rev. (Lett.)* 1972, **29**, 425
9 Krivanek, O. L. and Howie, A. *Acta. Cryst.* 1975, **8**, 213
10 Krivanek, O. L., Gaskell, P. H. and Howie, A. *Nature* 1976, **262**, 454
11 Yeh, G. S. Y. *J. Macro. Sci. (B)* 1972, **6**, 451
12 Ovchinnikov, Yu. K. and Markova, G. *Polym. Sci. USSR* 1967, **9**, 505
13 Howie, A., Krivanek, O. L. and Rudee, M. L. *Phil. Mag.* 1973, **27**, 235
14 Rudee, M. L. and Howie, A. *Phil. Mag.* 1972, **25**, 1001
15 Kralow, W., Ast, D. G., Goldfarb, W. and Siegel, B. M. *Phil. Mag.* 1976, **33**, 985
16 Uhlmann, D. R., Renninger, A. L., Kritchevsky, G. and

Vander Sande, J. *J. Macro. Sci. (B)* 1976, **12**, 153
17 Meyer, M., Vander Sande, J. and Ulhmann, D. R. *J. Polym. Sci.* 1978, **16**, 2005
18 Born, M. and Wolf, E. Principles of Optics, Pergamon, New York (1959)
19 Lenz, F. A. Electron Microscopy in Materials Science (Ed. U. Valdre), Academic Press, New York (1971)
20 Hanszen, K. Advances in Optical and Electron Microscopy, **4**, (Ed. R. Barer and V. E. Cosslett), Academic Press, London (1971)
21 Erickson, H. P. Advances in Optical and Electron Microscopy, **5**, (Ed. R. Barer and V. E. Cosslett), Academic Press, London (1973)
22 Cowley, J. M. Diffraction Physics, North-Holland, Amsterdam (1975)
23 Thon, F. *Phys. Blätter, Mosbach*, 1967, **23**, 450
24 Thon, F. and Siegel, B. M. *Ber, Bunsen, Ges.* 1970, **74**, 1116
25 Geil, P. H. *J. Macro. Sci. (B)* 1976, **12**, 173
26 Polk, D. E. *J. Non-Cryst. Solids* 1971, **5**, 365
27 Gibson, J. M., Howie, A. and Stobbs, W. M. *Inst. Phys. Conf.* 1977, **36**, 275
28 Krimm, S. *J. Phys. Chem.* 1953, **57**, 22
29 Parsons, D. F. *J. Appl. Phys.* 1972, **43**, 2885
30 Crick, R. A. and Misell, D. L. *J. Phys. (D)* 1971, **4**, 1
31 Bahr, G. F., Johnson, F. B. and Zeitler, E. *Lab. Invest.* 1965, **14**, 377
32 Veseley, D, Low, A. and Bevis, M. Developments in Electron Microscopy and Analysis (Ed. J. A. Venables), Academic Press, N. Y., 1975, 333
33 Krivanek, D. L. 6th European Congress on Electron Microscopy, Jerusalem, 275 (1976)
34 Cowley, J. M. *Acta Cryst. (A)* 1973, **29**, 529
35 Misell, D. L. *J. Phys. (A)* 1971, **4**, 798
36 Misell, D. L. and Atkins, A. J. *J. Phys. (A)* 1973, **6**, 218
37 Patterson, G. *J. Macromol. Sci. (B)* 1976, **12**, 61
38 Renninger, A. L., Wicks, G. G. and Uhlmann, D. R. *J. Polym. Sci.* 1975, **13**, 1247
39 Benoit, H. *J. Macromol. Sci. (B)* 1976, **12**, 27